INORGANIC CHEMISTRY FRONTIERS

RESEARCH ARTICLE

View Article Online
View Journal | View Issue

Cite this: *Inorg. Chem. Front.*, 2024, **11**, 2661

Adhesion, stability, structural and electronic properties of perovskite/$BaWO_4$ heterostructures: first-principles and experimental characterizations†

Yao Guo, [a] Shiding Zhang,*[a,b] Zhaoyu Zhang,[a] Yuanbin Xue,[a] Jianxin Li,[a] Haixiang Song,[a] Yuhua Wang *[b] and Qing Shen *[c]

The poor stability of lead halide perovskites poses a critical challenge for realizing potential applications. Constructing latticed-matched perovskite/$BaWO_4$ heterostructures is highly advantageous for achieving enhanced stability. However, there is limited knowledge about the interfacial properties. Herein, we conducted combined first-principles and experimental investigations of the perovskite/$BaWO_4$ heterostructures in this work. First, eight different interfacial configurations were constructed and investigated systematically. The influence of surface terminations on interfacial properties was examined through the adhesive strength and electronic structures. The results of adhesion work suggest that the $MAPbBr_3$/$BaWO_4$ configurations possess stronger interfacial interaction than the $CsPbBr_3$/$BaWO_4$ configurations. The formation of BaW/PbBr and BaW/MAPb configurations was more facile compared to their counterparts. The interfacial charge transfer direction, potential difference, and valence band edges of the perovskite/$BaWO_4$ heterostructures were found to be significantly influenced by the surface termination of $BaWO_4$. The absorption intensity of the perovskite/$BaWO_4$ heterostructures is significantly affected by the surface termination of the perovskite. Finally, the $CsPbBr_3$/$BaWO_4$ heterostructure was fabricated and characterized, thereby validating the first-principles predictions. This study provides a fundamental contribution to establishing perovskite/$BaWO_4$ heterostructures for the advancement of perovskite-based optoelectronic devices.

Received 24th January 2024,
Accepted 18th March 2024

DOI: 10.1039/d4qi00231h

rsc.li/frontiers-inorganic

1. Introduction

During the past decade, lead bromide perovskites in the guise of colloidal nanocrystals (NCs), such as cesium lead bromide ($CsPbBr_3$) and methylammonium lead bromide ($MAPbBr_3$), have been extensively explored for diverse applications, such as light-emitting diodes (LEDs) and photodetectors, owing to their distinctive photophysical characteristics including tunable band gap, high absorption coefficient, strong defect tolerance, high quantum yield, low fabrication cost, and so on.[1–5] Unfortunately, the excellent properties and exciting progress of lead bromide perovskite NCs are overshadowed by their limited operational lifetime under ambient conditions, which is severely hindering their real-world implementation and widespread adoption. The instability of perovskite NCs renders them vulnerable to environmental factors, which results in a series of detrimental effects, including structural alterations and phase transitions, reduced luminescence efficiency, and limited electron mobility.[6–10] An efficient way to enhance the stability of perovskite NCs and preserve their colloidal stability and photoluminescence is to couple them with another material to form a heterostructure.[11–16] Although perovskite NC heterostructures have been successfully designed to enhance their optical stability and emission intensity, their applications are still limited to a few combinations.[17–22] The design of perovskite NC heterostructures in combination with lattice-matched materials is still a topic that requires further investigation.

Barium tungstate ($BaWO_4$) with a scheelite structure is known for its high ionic/electronic conductivity and high thermal/chemical stability, and has potential applications in catalysis.[23–26] Recently, the heterostructural growth of $CsPbBr_3$

[a]School of Materials Science and Engineering, Anyang Institute of Technology, Anyang, 455000, China. E-mail: zsd@ayit.edu.cn
[b]Hubei Province Key Laboratory of System Science in Metallurgical Process, Wuhan University of Science and Technology, Wuhan, 430081, China. E-mail: wangyuhua@wust.edu.cn
[c]Faculty of Informatics and Engineering, The University of Electro-Communications, Tokyo, 182-8585, Japan. E-mail: shen@pc.uec.ac.jp

† Electronic supplementary information (ESI) available. See DOI: https://doi.org/10.1039/d4qi00231h

and $MAPbBr_3$ NCs on a $BaWO_4$ crystal was successfully demonstrated based on lattice matching.[27,28] Compared to the pure perovskite, the perovskite/$BaWO_4$ heterostructures exhibited enhanced luminescence intensity and sustained stability against UV-light radiation, heat, and diverse solvents. The $BaWO_4$ crystal can effectively inhibit halogen migration in the perovskite, leading to tunable emissions with different compositions. This implies the great potential of combining barium tungstate with lead bromide perovskite in advanced anticounterfeiting and encryption applications. To date, the $CsPbBr_3$/$BaWO_4$ and $MAPbBr_3$/$BaWO_4$ heterostructures have been examined by experimental investigations.[27,28] The interfacial characteristics of these heterostructures, which are directly determined by the arrangement of atoms and their interactions, are still not fully understood. Systematic and comparative investigations of the interfacial systems are therefore of great interest.[29–33] In this study, we utilize the first-principles approach to explore the heterostructures of $CsPbBr_3$/$BaWO_4$ and $MAPbBr_3$/$BaWO_4$. Moreover, the composition and morphological characteristics were further verified by microscopic and spectroscopic tools. The interfacial behavior and mechanism of the heterostructure were investigated by combining theoretical and experimental approaches to assess the photocatalytic potential of these newly developed heterostructures.

2. Computational and experimental details

The first-principles density functional theory (DFT) calculations were carried out based on projector augmented wave (PAW) formalism[34] within the Vienna *ab initio* simulation package (VASP, version 5.4.4).[35–37] The exchange correlation effect was evaluated by means of the generalized gradient approximation (GGA) of the Perdew–Burke–Ernzerhof (PBE) functional.[38] The kinetic plane wave energy cutoff was set to 450 eV with Gaussian smearing (σ = 0.1 eV).[39] Brillouin-zone integration was done using the Monkhorst–Pack[40] k-point mesh with 0.02 $Å^{-1}$ separation. The vacuum layer thickness was set to 15 Å to neglect the coupling between the images. The spurious interactions between periodic images were significantly reduced by using the dipole correction in the VASP (IDIPOL = 3). The DFT-D3 with the BJ-damping method[41] was included to consider the van der Waals (vdW) interactions. The convergence criteria for energy and force were 10^{-6} eV and 0.005 eV $Å^{-1}$, respectively. During the geometric optimizations, the bottom layers were constrained to the bulk geometry, while the remaining layers were fully relaxed. The VESTA (Visualization for Electronic and Structural Analysis) program[42] was utilized to visualize the crystallographic, volumetric, and morphological data.

In this study, we adopted the cubic structure (space group $Pm\bar{3}m$) for $CsPbBr_3$, the monoclinic (space group $P2_1/m$) structure for $MAPbBr_3$, and the tetragonal (space group $I4_1/a$) structure for $BaWO_4$. The atomic structures and lattice parameters derived from first-principles simulations are provided in Fig. S1 and Table S1,† exhibiting excellent agreement with the corresponding experimental results.[43–45] Following the rigorous lattice matching principle, the (200) in-plane lattice spacing in $BaWO_4$ closely matched those of $CsPbBr_3$ and $MAPbBr_3$, serving as the foundation for constructing the perovskite/$BaWO_4$ heterostructures. The perovskite (200) slabs were constructed employing a stoichiometric six-layer slab, while the $BaWO_4$ (200) slab was generated using an eleven-layer symmetric slab. $CsPbBr_3$ (or $MAPbBr_3$) exhibits two potential surface terminations: the termination by Cs (or MA) cations, and the termination by Pb cations. In contrast, the $BaWO_4$ slab features two distinct surface types: BaW- and O-terminated surfaces. By combining the perovskite and $BaWO_4$ slabs, we generated a total of eight lattice-matched interfacial configurations, as depicted in Fig. 1. The lattice parameters and mean absolute strain values for the eight models are presented in Table S2.†

The $CsPbBr_3$/$BaWO_4$ heterostructure was prepared through an *in situ* synthesis thermal-assisted method. The stoichiometric proportions of $Na_2WO_4{\cdot}2H_2O$ (1 mmol) and $Ba(NO_3)_2$ (1 mmol) were dissolved in a 20 ml aqueous solution and stirred in a 50 ml beaker, immediately resulting in a white $BaWO_4$ precipitate. After centrifugation and drying, 145 mg of the precipitate was weighed and put together with $PbBr_2$ (0.8 mmol) into a three-neck flask with 20 ml of octadecene as the solvent, then heated to 120 °C with nitrogen protection; the air and water impurities in the three-neck flask were extracted. The reaction mixture was kept for 30 min, heated up to 180 °C, and immediately infused with 3 ml of Cs-OA to obtain a yellow solution, which was reacted for 10 seconds. The solution was cooled to room temperature with a cold-water bath, and the precipitates were centrifuged and washed with *n*-hexane three times, toluene twice, anhydrous ethanol once, and finally vacuum dried at 60 °C for 8 hours, to obtain the $CsPbBr_3$/$BaWO_4$ heterostructure.

3. Results and discussion

3.1. Interfacial adhesion

The work of adhesion (W_{ad})[46–48] is commonly employed to characterize the interfacial stability and bonding strength. The work of interfacial adhesion can be described as the reversible energy necessary to divide the heterostructure into two free surfaces, quantified by the following equation:

$$W_{ad} = [E_{PVK} + E_{BWO} - E_{total}]/A \quad (1)$$

where E_{PVK} and E_{BWO} correspond to the total energy of the fully relaxed perovskite and $BaWO_4$ slabs, respectively. E_{total} represents the total energy of the perovskite/$BaWO_4$ interface, while A specifies the interface area. It is widely accepted that a higher W_{ad} value corresponds to enhanced bonding strength. The calculated W_{ad} values of the $CsPbBr_3$/$BaWO_4$ and $MAPbBr_3$/$BaWO_4$ heterostructures are compared in Table 1. The formation of all eight observed interfacial configurations is facilitated by the positive adhesion work. The perovskite/

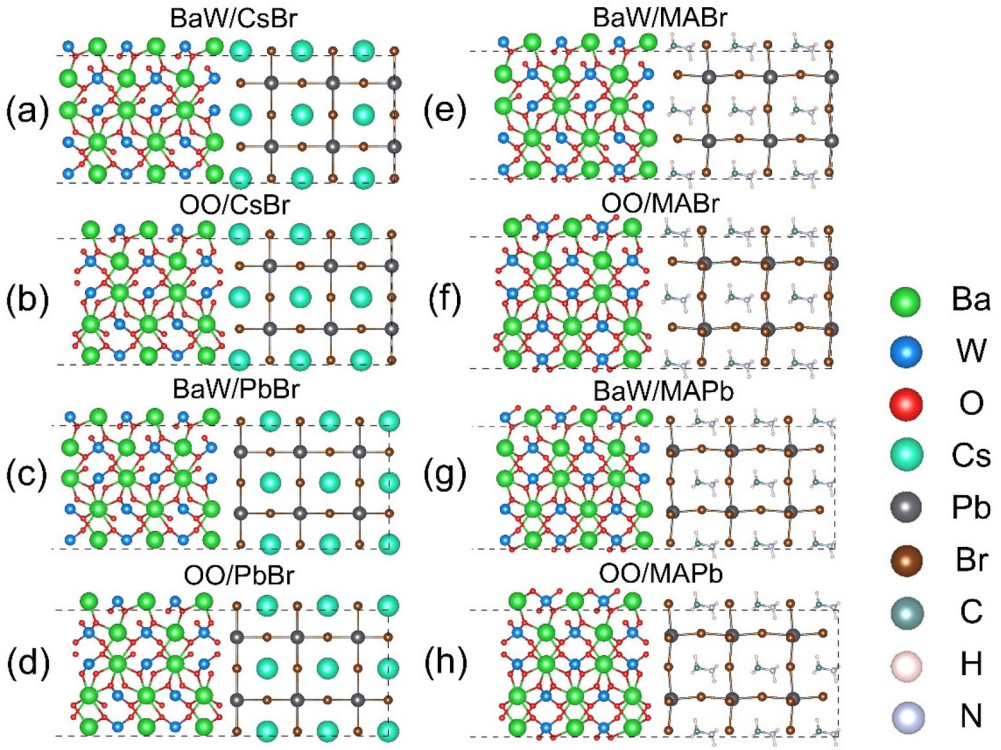

Fig. 1 Schematic illustration of the perovskite/$BaWO_4$ interfaces: (a) BaW/CsBr, (b) OO/CsBr, (c) BaW/PbBr, (d) OO/PbBr, (e) BaW/MABr, (f) OO/CsBr, (g) BaW/MAPb, and (h) OO/MAPb.

Table 1 Calculated adhesion work (eV $Å^{-2}$), charge transfer (e), plane-averaged electrostatic potential difference (eV) and work function (eV) of the relaxed perovskite/$BaWO_4$ interfaces

Interface	Adhesion work	Charge transfer[a]	Potential difference	Work function
BaW/CsBr	0.018	−0.2	2.0	2.8
OO/CsBr	0.024	2.0	1.0	6.7
BaW/PbBr	0.035	−1.5	2.0	2.6
OO/PbBr	0.008	1.8	1.0	6.5
BaW/MABr	0.036	−0.6	1.0	2.8
OO/MABr	0.014	0.7	−0.5	6.7
BaW/MAPb	0.052	−1.4	1.0	2.5
OO/MAPb	0.026	1.9	−0.5	6.7

[a] The positive values indicate charge transfer from perovskite to $BaWO_4$, whereas the negative values exhibit charge transfer from $BaWO_4$ to perovskite.

$BaWO_4$ interface exhibits larger W_{ad} values when compared to the weak perovskite/MXene system,[30] while exhibiting equivalent W_{ad} values to the strong perovskite/Ga_2O_3 system,[31] thereby suggesting a high degree of interface stability. Among them, the $MAPbBr_3/BaWO_4$ interface exhibits larger W_{ad} values, ranging from 0.014 to 0.052 eV $Å^{-2}$, when compared to those of the $CsPbBr_3/BaWO_4$ interface, which span from 0.008 to 0.035 eV $Å^{-2}$. This comparison further suggests that the $MAPbBr_3/BaWO_4$ structure possesses a relatively higher degree of stability. The comprehensive investigations indicate that the W_{ad} values at the interfaces between BaW- and Pb-terminations are higher compared to the other three interfaces, regardless of $CsPbBr_3/BaWO_4$ and $MAPbBr_3/BaWO_4$. Therefore, the formation of BaW/PbBr and BaW/MAPb interfaces was more facile compared to their counterparts in experiments. The stability of the interface correlates with the extent of atomic rearrangement.

To clarify the bonding mechanism in the perovskite/$BaWO_4$ heterostructures, the electron localization function (ELF),[49] as well as the atomic structures of $CsPbBr_3/BaWO_4$ and $MAPbBr_3/BaWO_4$ systems, was analyzed, as shown in Fig. 2. In the colorimetric representation of electron localization, red is used to represent electrons with a high degree of localization, while blue is used to represent electrons with a high degree of delocalization. Localization and delocalization represent the spatial distribution patterns of electrons within the system. Localization signifies the concentration of electron density in specific regions, whereas delocalization denotes the free movement of electrons throughout the system, indicating enhanced electron mobility. The nearly spherical electron distribution indicates the strong ionic bonding character between Pb and Br atoms. In contrast, the $BaWO_4$ side exhibits the covalent bonding for the WO_4 anions and the ionic bonding character for the Ba cations. The $MAPbBr_3/BaWO_4$ configurations with less blue area in the interface region indicate stronger interfacial interaction than the $CsPbBr_3/BaWO_4$ configurations. Upon closer inspection of the interface region, noticeable distortions of the Pb-Br_6 octahedra in the cubic structure can be observed.[50] These distortions are attributed to the strong inter-

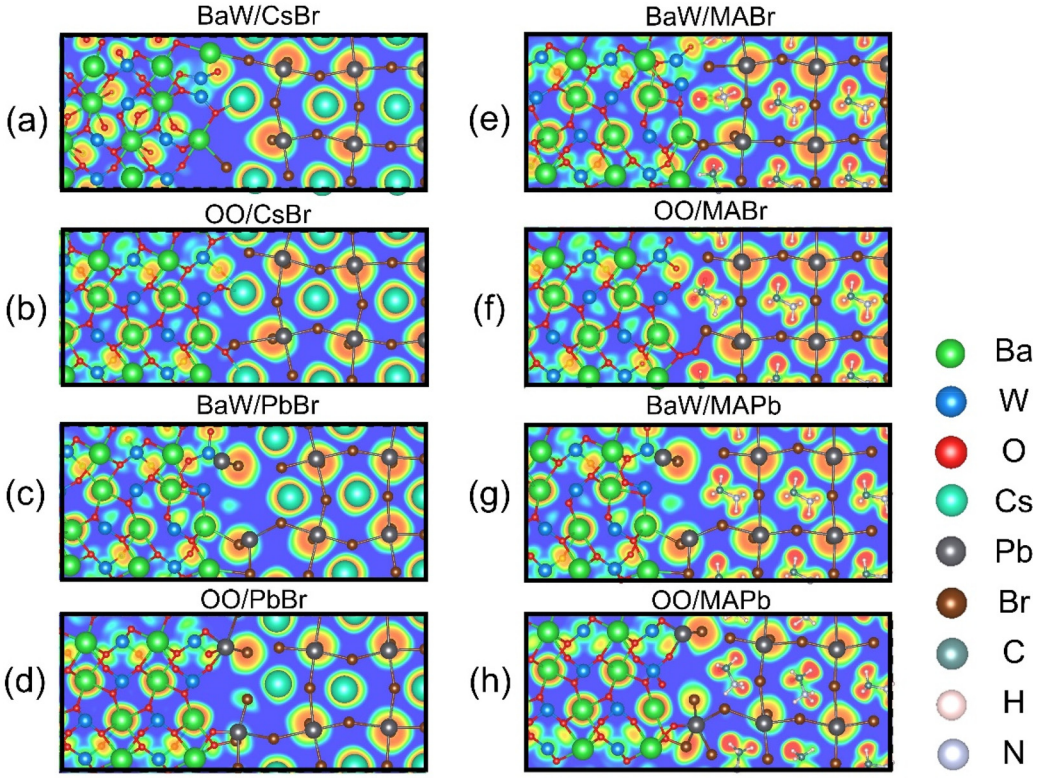

Fig. 2 ELF of the relaxed perovskite/$BaWO_4$ interfaces: (a) BaW/CsBr, (b) OO/CsBr, (c) BaW/PbBr, (d) OO/PbBr, (e) BaW/MABr, (f) OO/CsBr, (g) BaW/MAPb, and (h) OO/MAPb.

actions between $BaWO_4$ and perovskite. Moreover, the $CsPbBr_3/BaWO_4$ configurations undergo more significant distortions compared to the $MAPbBr_3/BaWO_4$ configurations. Among the various terminations, the BaW/PbBr and BaW/MAPb configurations with the highest W_{ad} values demonstrate more significant distortions compared to their counterparts, which is coincident with the results in Table 1. To provide a quantitative measure of charge transfer between perovskite and $BaWO_4$, we conducted Bader charge analysis[51] on representative atoms. The values of calculated charge transfer are presented in Table 1. The charge transfer direction is significantly influenced by the surface termination, irrespective of the $CsPbBr_3/BaWO_4$ or $MAPbBr_3/BaWO_4$ systems. Specifically, the BaW/perovskite (BaW/CsBr, BaW/PbBr, BaW/MABr, and BaW/MAPb) configurations exhibit electron transfer from $BaWO_4$ to the perovskite layer, whereas the OO/perovskite (OO/CsBr, OO/PbBr, OO/MABr, and OO/MAPb) configurations indicate charge transfer from the perovskite to the $BaWO_4$ layer. The above results can be attributed to the interfacial bonding between perovskite and $BaWO_4$.

3.2. Electronic structures

To thoroughly elucidate the intricate characteristics of interface coupling and charge redistribution within the perovskite/$BaWO_4$ heterostructures, we explored the *z*-axis dependence of the three-dimensional and plane-averaged charge density difference ($\Delta\rho$).[52] The yellow-colored segment signifies charge accumulation, whereas the cyan-colored segment denotes charge depletion. Fig. 3 suggests that the interface region is the primary site for charge transfer and redistribution. The magnitude of the charge distribution at the interface is significantly influenced by the strength of the interfacial interaction. The BaW/PbBr and BaW/MAPb configurations exhibit denser electron isosurfaces compared to the other configurations, consistent with their highest W_{ad} values listed in Table 1. The plane-averaged charge density difference curves obtained from isosurfaces exhibit distinct trends depending on various surface terminations. The curves of the OO/perovskite (OO/CsBr, OO/PbBr, OO/MABr, and OO/MAPb) configurations exhibit a similar pattern, with electron accumulation on the $BaWO_4$ side and depletion on the perovskite side, indicating a distinct contrast at the interface. In contrast, the curves of BaW/perovskite (BaW/CsBr, BaW/PbBr, BaW/MABr, and BaW/MAPb) configurations display an irregular distribution, signifying complex charge redistribution at the interface regions. The above results are entirely consistent with the direction of charge transfer presented in Table 1. The OO/perovskite configurations are bonded with the Cs–O and Pb–O bonds. Such configurations under O-rich conditions contain more interfacial bonds and exhibit distinct charge redistributions at the interface. The accumulation of various carriers at the interfaces on both ends of the heterointerface leads to the formation of a built-in electric field, which is directed from the hole accumulation region to the electron accumulation area.[53]

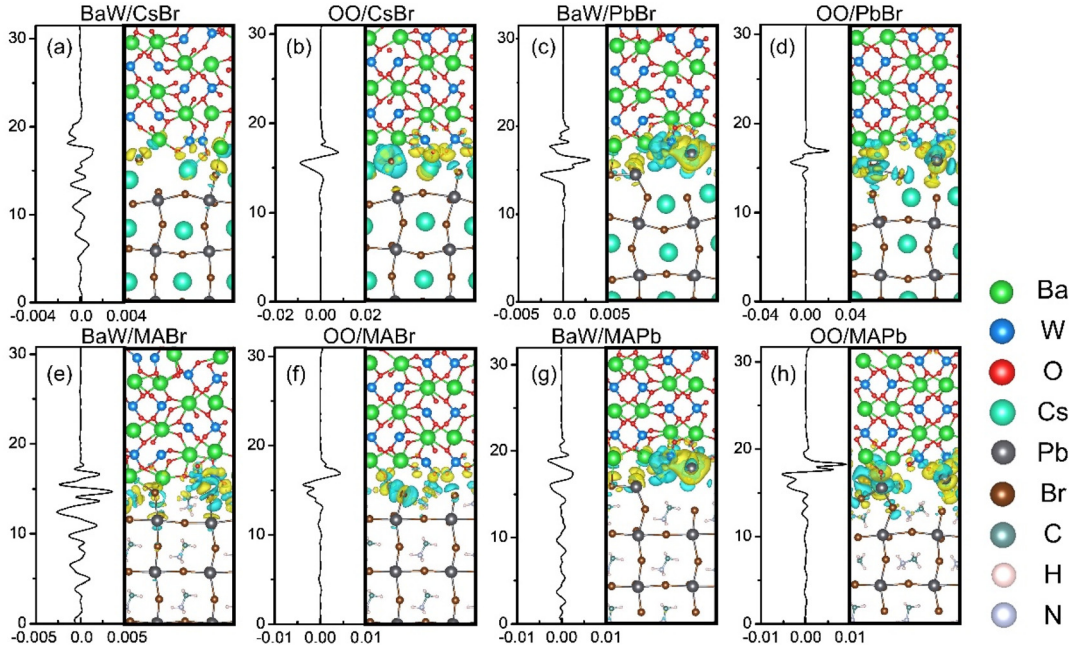

Fig. 3 Plane-averaged electron density difference $\Delta\rho(z)$ and 3D charge density difference (0.002 e Å^{-3}) of the relaxed perovskite/$BaWO_4$ interfaces: (a) BaW/CsBr, (b) OO/CsBr, (c) BaW/PbBr, (d) OO/PbBr, (e) BaW/MABr, (f) OO/CsBr, (g) BaW/MAPb, and (h) OO/MAPb.

To offer a comprehensive assessment of electronic transport behavior at the perovskite/$BaWO_4$ heterostructures, the plane-averaged electrostatic potentials in the vertical direction were analyzed and are plotted in Fig. 4. The band alignment and the work function of the perovskite/$BaWO_4$ heterostructures can be estimated *via* the electrostatic potentials.[54] Evaluation of the potential offset and work function of the heterostructures is based on the theoretical framework of the plane-averaged electrostatic potentials. When two distinct surfaces come into contact and create heterostructures, the disparity in Fermi energy leads to electron transport at the heterointerface, resulting in band offsets. As shown in Fig. 4, a notable contrast exists in the atomic arrangements of perovskite and $BaWO_4$, with atoms near the interface undergoing substantial migration toward their final stable state, ultimately leading to a macroscopic discrepancy in the plane-averaged electrostatic potentials. The plane-averaged electrostatic potential difference (ΔV) between the perovskite and $BaWO_4$ was estimated and is summarized in Table 1. The positive value indicates that the plane-averaged potentials of the $BaWO_4$ side are higher than those at the perovskite side. The potential offset, influenced by the atomic configurations near the interface, plays a crucial role in shaping the electronic barrier and ultimately affects the device performance.[55] The BaW/perovskite configurations display greater ΔV compared to the OO/perovskite configurations, irrespective of whether $CsPbBr_3$ or $MAPbBr_3$ is involved. Simultaneously, the $CsPbBr_3/BaWO_4$ configurations show a larger ΔV compared to the $MAPbBr_3/BaWO_4$ configurations. In particular, for the OO/MABr and OO/MAPb configurations, negative ΔV values are observed, indicating a reversal in the potential offset. The work function signifies the minimum energy needed to extract electrons from the Fermi level to reach the vacuum level. Table 1 details the work functions of the corresponding perovskite/$BaWO_4$ heterostructures. Importantly, the work functions of the OO/perovskite configurations undergo substantial modulation towards higher values, presenting a stark contrast to the work function observed in the BaW/perovskite configurations. The results of potential differences and work function measurements exhibit a high degree of consistency with the charge transfer data outlined in Table 1. The considerably altered work function indicates that surface engineering holds promise as an effective approach for achieving ohmic contact of n- and p-type.

The density of states (DOS) provides a quantitative description of the electronic states in different orbitals, which is essential for a comprehensive understanding of the interfacial bonding mechanism. For a more in-depth exploration of the perovskite/$BaWO_4$ heterostructures, we calculated and depicted the atom-projected DOS in Fig. 5. More details of the calculated DOS for $CsPbBr_3$, $MAPbBr_3$, and $BaWO_4$ in the bulk phase are plotted in Fig. S2.† As a member of the scheelite family, $BaWO_4$ has a larger band gap compared to $CsPbBr_3$ (or $MAPbBr_3$).[56] The calculated DOS of the perovskite/$BaWO_4$ heterostructures shows that the top of the valence band is entirely composed of O 2p and Br 4p orbitals while the bottom of the conduction band is dominated by the W 5d orbitals. The formation of the perovskite/$BaWO_4$ heterointerface is a consequence of the hybridization of Br 4p and W 5d states. The eight different interfacial configurations exhibit similar DOS features. The OO/perovskite configurations are identified as belonging to a type-II heterostructure, with the conduction band minimum (CBM) contributed by the perovskite and the

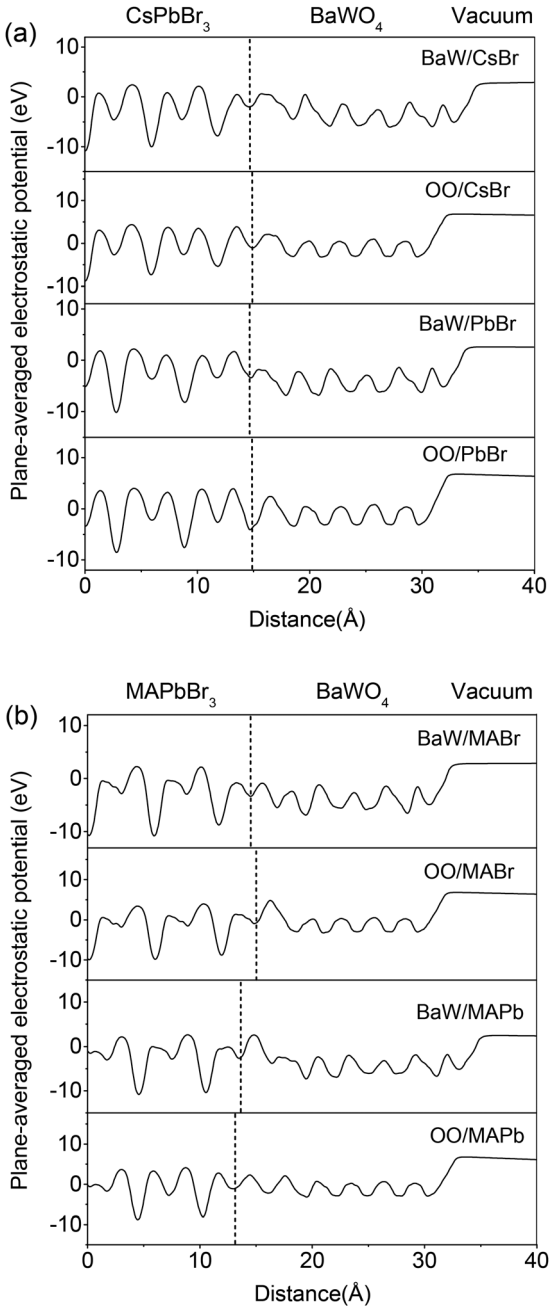

Fig. 4 Plane-averaged electrostatic potential of the relaxed perovskite/$BaWO_4$ interfaces: (a) $CsPbBr_3/BaWO_4$ and (b) $MAPbBr_3/BaWO_4$.

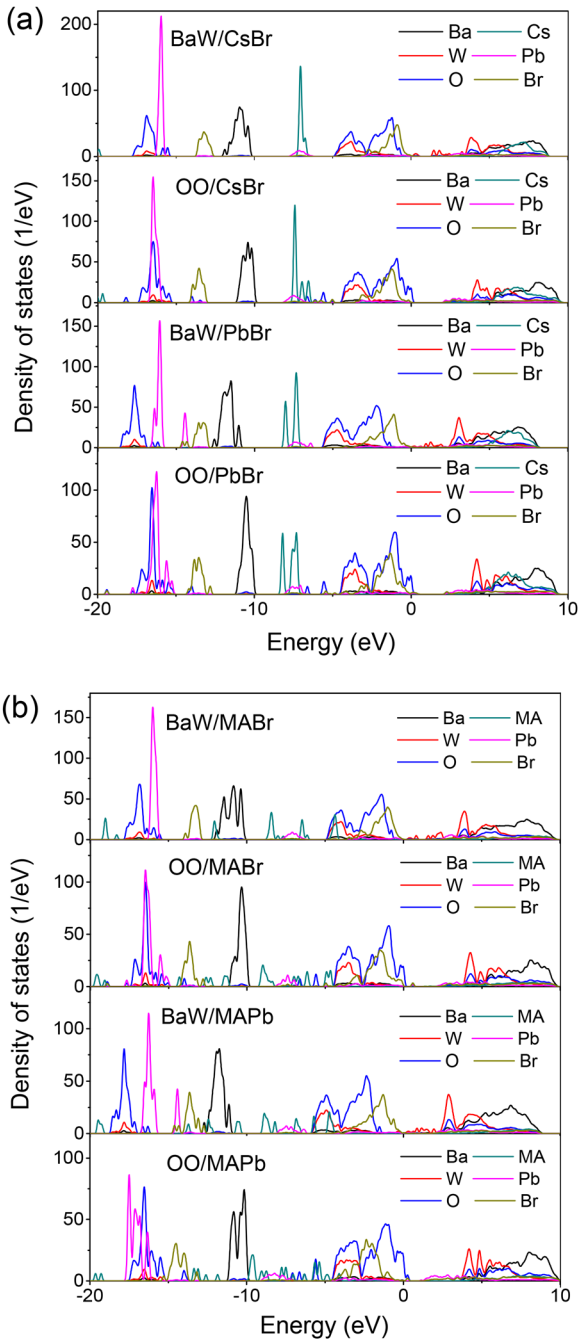

Fig. 5 DOS of the relaxed perovskite/$BaWO_4$ interfaces: (a) $CsPbBr_3/BaWO_4$ and (b) $MAPbBr_3/BaWO_4$.

valence band maximum (VBM) contributed by $BaWO_4$. A close examination of the top of the valence band reveals that the O 2p and peaks move toward the lower energy region for the BaW/perovskite configurations. In particular, the BaW/PbBr and BaW/MAPb configurations exhibit the largest peak shift,[57] suggesting enhanced binding energy between the two materials at the interface. The observation of interfacial defect states across the band gap of the BaW/perovskite configurations also suggests that hybridization is enhanced at the interface. Hence, the typical type-II band alignment observed in the OO/perovskite configurations was transformed into the typical type-I band alignment in the BaW/perovskite configurations. This is consistent with the results of charge transfer, potential difference and work function as outlined in Table 1. The findings imply that the electronic structures of the perovskite/$BaWO_4$ heterostructures are dependent on the surface termination of $BaWO_4$, not that of perovskite. The surface termination of $BaWO_4$ has crucial potential significance in the transformation of a type-I heterostructure to a type-II heterostructure.

3.3. Optical properties

The light absorption coefficient of the perovskite/$BaWO_4$ heterostructures is a key parameter for evaluating their optical response to sunlight. The absorption spectra of the $CsPbBr_3$/$BaWO_4$ and $MAPbBr_3$/$BaWO_4$ heterostructures are calculated and displayed as in Fig. 6. For comparison, the light absorption spectra of $CsPbBr_3$, $MAPbBr_3$, and $BaWO_4$ in the bulk phase were calculated, which are shown in Fig. S3.† The shapes of the absorption curves of $CsPbBr_3$/$BaWO_4$ and $MAPbBr_3$/$BaWO_4$ heterostructures are quite similar. The optical absorption spectrum of the heterostructures shows three distinct peaks at 3.5, 5.5, and 9.5 eV. The first peak at 3.5 eV is primarily due to the transition from Br 4p to Pb 6p states between the conduction and valence bands.[58] The second peak around 5.5 eV is attributed to the optical transition from O 2p orbitals to W 5d orbitals. The third peak around 9.5 eV originates from the transition from hybridized W 5d and O 2p states to W 5d states.[59] A close inspection of the absorption spectra reveals that the absorption intensity of the perovskite exhibits a similar trend for both $CsPbBr_3$/$BaWO_4$ (BaW/CsBr > OO/CsBr > BaW/PbBr > OO/PbBr) and $MAPbBr_3$/$BaWO_4$ (BaW/MABr > OO/MABr > BaW/MAPb > OO/MAPb). The BaW/CsBr heterostructure (or BaW/MABr) exhibits the lowest interfacial distortion and remarkably well-preserved perovskite-type structures, leading to a significantly higher absorption coefficient. These results suggest that the optical properties of the perovskite/$BaWO_4$ heterostructures are significantly affected by the surface termination of the perovskite layers, but not the $BaWO_4$ layers. To improve the device performance through interface modification, focusing on the perovskite layer should be a promising strategy.

3.4. Experimental verification

The $CsPbBr_3$/$BaWO_4$ heterostructure was successfully fabricated to further verify the first-principles predictions. The X-ray diffraction (XRD) patterns of $CsPbBr_3$, $BaWO_4$, and $CsPbBr_3$/$BaWO_4$ are displayed in Fig. 7. The XRD pattern showed diffraction peaks at 2θ values of 15.1°, 21.3°, 30.6°, 37.7°, and 43.6° corresponding to the (100), (110), (200), (211), and (220) phases of the typical cubic $CsPbBr_3$, respectively.[60,61] In addition, the diffraction peaks at 17.3°, 27.9°, 31.7°, 42.8°, 45.6°, and 53.5° are attributed to the (101), (112), (200), (204), (220), and (312) phases of the tetragonal $BaWO_4$, respectively.[62] All diffraction peaks are consistent with the crystalline phase of $CsPbBr_3$ (JCPDS No. 18-0364) and $BaWO_4$ (JCPDS No. 43-0646). The results showed that $CsPbBr_3$ and $BaWO_4$ exhibited high crystallinity with well-maintained cubic perovskite and

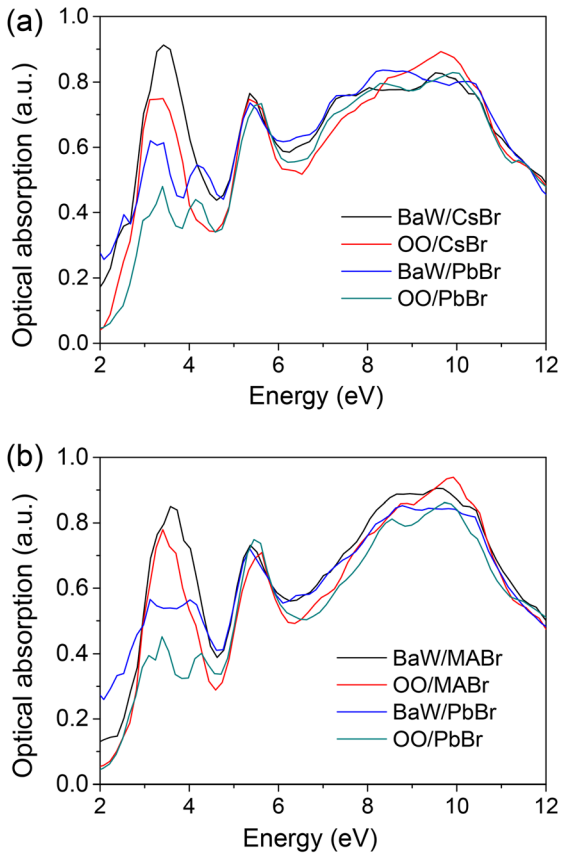

Fig. 6 Absorption coefficients of the relaxed perovskite/$BaWO_4$ interfaces: (a) $CsPbBr_3$/$BaWO_4$ and (b) $MAPbBr_3$/$BaWO_4$.

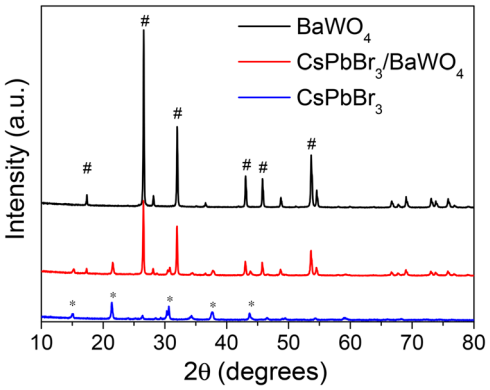

Fig. 7 Experimental XRD patterns of $CsPbBr_3$, $BaWO_4$, and $CsPbBr_3$/$BaWO_4$.

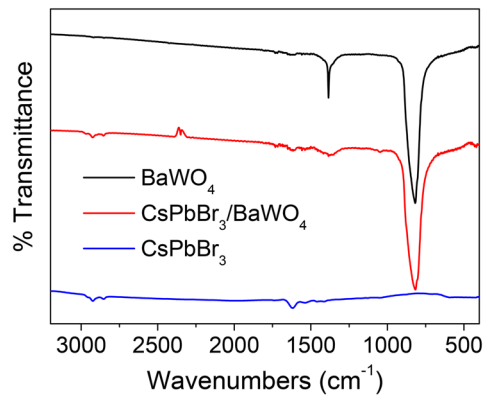

Fig. 8 FT-IR patterns of $CsPbBr_3$, $BaWO_4$, and $CsPbBr_3$/$BaWO_4$.

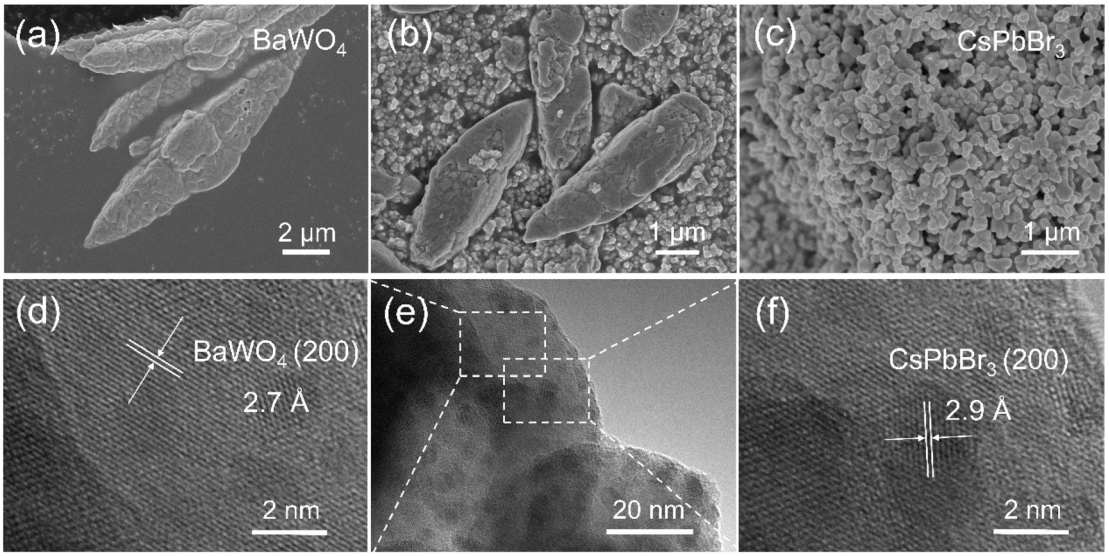

Fig. 9 SEM images of (a) $BaWO_4$, (b) $CsPbBr_3/BaWO_4$, and (c) $CsPbBr_3$; TEM images of (d) $BaWO_4$, (e) $CsPbBr_3/BaWO_4$, and (f) $CsPbBr_3$.

tetragonal scheelite crystal phases during the formation of the $CsPbBr_3/BaWO_4$ heterostructures.

To evaluate the chemical bond formation and interactions, FT-IR spectral analysis of $CsPbBr_3$, $BaWO_4$, and $CsPbBr_3/BaWO_4$ was performed and the results are displayed in Fig. 8. The spectrum of $BaWO_4$ reveals a vibrational mode at 820 cm^{-1}, associated with asymmetric W–O vibrations, thereby confirming the presence of the typical WO_4 in the prepared $BaWO_4$ material.[63,64] The additional absorption peak of $BaWO_4$ around 1400 cm^{-1} may be attributed to the stretching vibrations of the organic groups present in the precursor. Two small peaks are recognized around 1600 and 2900 cm^{-1} in the spectrum of $CsPbBr_3$. The peak at 1600 cm^{-1} can be assigned to the N–H bending vibrations of the ligands, whereas the peak at 2900 cm^{-1} is associated with the oleyl group.[65] The FT-IR analysis confirms the formation of the $CsPbBr_3/BaWO_4$ heterostructures.

The structural features of the prepared $CsPbBr_3/BaWO_4$ heterostructures were carefully identified by scanning electron microscopy (SEM) and transmission electron microscopy (TEM), as demonstrated in Fig. 9. The TEM images clearly depict the $CsPbBr_3$ and $BaWO_4$ materials. Specifically, the analysis indicates that the interplanar spacings of 2.9 Å correspond to the $CsPbBr_3$ (200) plane,[66] whereas the interplanar spacings of 2.7 Å correspond to the $BaWO_4$ (200) plane,[67] respectively. The confirmation of lattice-matched growth between $CsPbBr_3$ and $BaWO_4$ is intricately validated through TEM observations, closely aligning with the predictions derived from first-principles calculations.

4. Conclusions

To summarize, first-principles and experimental studies were employed to investigate the interfacial properties between perovskite and $BaWO_4$. The interfacial properties include atomic arrangement, adhesion work, charge redistribution, potential difference, work function, and their orbital hybridization, as well as their optical absorption. The results indicate that the $MAPbBr_3/BaWO_4$ configurations possess stronger interfacial interaction than the $CsPbBr_3/BaWO_4$ configurations. The formation of BaW/PbBr and BaW/MAPb configurations was more facile compared to their counterparts. Our study highlights the importance of surface termination for the interfacial properties. The interfacial charge transfer direction, potential difference, and band alignment of the perovskite/$BaWO_4$ heterostructures were found to be significantly influenced by the surface termination of $BaWO_4$. The absorption intensity of the perovskite/$BaWO_4$ heterostructures is significantly affected by the surface termination of the perovskite. The lattice-matching growth of $CsPbBr_3/BaWO_4$ was achieved and the existence of the heterostructure was confirmed by XRD, SEM, and TEM characterization. This study helps us to gain better insight into the nature of the perovskite/$BaWO_4$ heterostructures, thereby laying the groundwork for the realization of high-performance perovskite-based devices.

Conflicts of interest

The authors declare that they have no known competing financial interests or personal relationships that could have appeared to influence the work reported in this paper.

Acknowledgements

This work was supported by the National Natural Science Foundation of China (Grant No. 12381240132), the China Scholarship Council (Grant No. 202308410380), the

Postgraduate Education Reform and Quality Improvement Project of Henan Province (Grant No. YJS2023JD60), and the Henan International Joint Laboratory of Nanocomposite Sensing Materials.

References

1 S. R. Smock, Y. Chen, A. J. Rossini and R. L. Brutchey, The surface chemistry and structure of colloidal lead halide perovskite nanocrystals, *Acc. Chem. Res.*, 2021, **54**(3), 707–718.
2 P. Liu, W. Chen, W. Wang, B. Xu, D. Wu, J. Hao, W. Cao, F. Fang, Y. Li, Y. Zeng, R. Pan, S. Chen, W. Cao, X. W. Sun and K. Wang, Halide-rich synthesized cesium lead bromide perovskite nanocrystals for light-emitting diodes with improved performance, *Chem. Mater.*, 2017, **29**(12), 5168–5173.
3 G. Xiao, Y. Cao, G. Qi, L. Wang, C. Liu, Z. Ma, X. Yang, Y. Sui, W. Zheng and B. Zou, Pressure effects on structure and optical properties in cesium lead bromide perovskite nanocrystals, *J. Am. Chem. Soc.*, 2017, **139**(29), 10087–10094.
4 Y. Cai, W. Li, D. Tian, S. Shi, X. Chen, P. Gao and R.-J. Xie, Organic sulfonium-stabilized high-efficiency cesium or methylammonium lead bromide perovskite nanocrystals, *Angew. Chem., Int. Ed.*, 2022, **61**(37), e202209880.
5 S. Wang, A. A. Yousefi Amin, L. Wu, M. Cao, Q. Zhang and T. Ameri, Perovskite nanocrystals: Synthesis, stability, and optoelectronic applications, *Small Struct.*, 2021, **2**(3), 2000124.
6 G. H. Ahmed, J. Yin, O. M. Bakr and O. F. Mohammed, Successes and challenges of core/shell lead halide perovskite nanocrystals, *ACS Energy Lett.*, 2021, **6**(4), 1340–1357.
7 C. Otero-Martínez, N. Fiuza-Maneiro and L. Polavarapu, Enhancing the intrinsic and extrinsic stability of halide perovskite nanocrystals for efficient and durable optoelectronics, *ACS Appl. Mater. Interfaces*, 2022, **14**(30), 34291–34302.
8 K. Xing, S. Cao, X. Yuan, R. Zeng, H. Li, B. Zou and J. Zhao, Thermal and photo stability of all inorganic lead halide perovskite nanocrystals, *Phys. Chem. Chem. Phys.*, 2021, **23**(32), 17113–17128.
9 M. Liu, Q. Wan, H. Wang, F. Carulli, X. Sun, W. Zheng, L. Kong, Q. Zhang, C. Zhang, Q. Zhang, S. Brovelli and L. Li, Suppression of temperature quenching in perovskite nanocrystals for efficient and thermally stable light-emitting diodes, *Nat. Photonics*, 2021, **15**(5), 379–385.
10 C. Zhang, S. Wang, X. Li, M. Yuan, L. Turyanska and X. Yang, Core/shell perovskite nanocrystals: Synthesis of highly efficient and environmentally stable $FAPbBr_3$/$CsPbBr_3$ for LED applications, *Adv. Funct. Mater.*, 2020, **30**(31), 1910582.
11 S. Bera and N. Pradhan, Perovskite nanocrystal heterostructures: Synthesis, optical properties, and applications, *ACS Energy Lett.*, 2020, **5**(9), 2858–2872.
12 A. Kipkorir, J. DuBose, J. Cho and P. V. Kamat, $CsPbBr_3$–CdS heterostructure: Stabilizing perovskite nanocrystals for photocatalysis, *Chem. Sci.*, 2021, **12**(44), 14815–14825.
13 L. Ruan and Y. Zhang, NIR-excitable heterostructured upconversion perovskite nanodots with improved stability, *Nat. Commun.*, 2021, **12**(1), 219.
14 C. Yuan, Y. He, R. Chen, Y. Sun, J. Li, W. Cui, P. Chen, J. Sheng and F. Dong, Perovskite nanocrystals-based heterostructures: synthesis strategies, interfacial effects, and photocatalytic applications, *Sol. RRL*, 2021, **5**(2), 2000419.
15 L. Rao, Q. Zhang, B. Sun, M. Wen, J. Zhang, S. Yu, T. Fu and X. Niu, $CsPbBr_3$/Cs_4PbBr_6 heterostructure solids with high stability and photoluminescence for white light-emitting diodes, *J. Alloys Compd.*, 2022, **919**, 165857.
16 S. Wang, C. Bi, A. Portniagin, J. Yuan, J. Ning, X. Xiao, X. Zhang, Y. Y. Li, S. V. Kershaw, J. Tian and A. L. Rogach, $CsPbI_3$/PbSe heterostructured nanocrystals for high-efficiency solar cells, *ACS Energy Lett.*, 2020, **5**(7), 2401–2410.
17 L. Ruan and Y. Zhang, Upconversion perovskite nanocrystal heterostructures with enhanced luminescence and stability by lattice matching, *ACS Appl. Mater. Interfaces*, 2021, **13**(43), 51362–51372.
18 L. Zhang, Y. Liu, Y. He, X. Zhang, C. Geng, R. Yang and S. Xu, Stable $CsPbX_3$/ZnO heterostructure nanocrystals for light-emitting application, *J. Phys. Chem. Lett.*, 2021, **12**(45), 10953–10957.
19 Q. Zhang, Y. Zhou, Y. Wei, M. Tai, H. Nan, Y. Gu, J. Han, X. Yin, J. Li and H. Lin, Improved phase stability of γ-$CsPbI_3$ perovskite nanocrystals using the interface effect using iodine modified graphene oxide, *J. Mater. Chem. C*, 2020, **8**(7), 2569–2578.
20 M. Imran, L. Peng, A. Pianetti, V. Pinchetti, J. Ramade, J. Zito, F. Di Stasio, J. Buha, S. Toso, J. Song, I. Infante, S. Bals, S. Brovelli and L. Manna, Halide perovskite–lead chalcohalide nanocrystal heterostructures, *J. Am. Chem. Soc.*, 2021, **143**(3), 1435–1446.
21 J. Ghosh, L. P. L. Mawlong, G. B. Manasa, A. J. Pattison, W. Theis, S. Chakraborty and P. K. Giri, Solid-state synthesis of stable and color tunable cesium lead halide perovskite nanocrystals and the mechanism of high-performance photodetection in a monolayer MoS_2/$CsPbBr_3$ vertical heterojunction, *J. Mater. Chem. C*, 2020, **8**(26), 8917–8934.
22 S. Gull and G. Li, Deep red emission from Cs_4PbI_6/$CsPbI_3$/ZnS heterostructure for enhanced stability and photoluminescence quantum yield, *Ceram. Int.*, 2023, **49**(4), 5915–5921.
23 D. Sivaganesh, S. Saravanakumar, V. Sivakumar, R. Sangeetha, L. J. Berchmans, K. S. S. Ali and A. M. Alshehri, Effect of preparation techniques on $BaWO_4$: Structural, morphological, optical and electron density distribution analysis, *J. Mater. Sci.: Mater. Electron.*, 2021, **32**(2), 1466–1475.
24 A. Azzouzi, M. Benchikhi and R. El Ouatib, Room-temperature co-precipitation synthesis of (Ca,Sr,Ba)WO_4 solid solutions: Structural refinement, morphology and band gap tuning, *Ceram. Int.*, 2020, **46**(15), 23706–23718.
25 M. Kowalkińska, P. Głuchowski, T. Swebocki, T. Ossowski, A. Ostrowski, W. Bednarski, J. Karczewski and A. Zielińska-

Jurek, Scheelite-type wide-bandgap ABO_4 compounds (A = Ca, Sr, and Ba; B = Mo and W) as potential photocatalysts for water treatment, *J. Phys. Chem. C*, 2021, **125**(46), 25497–25513.

26 S. Tang, S. Wang, X. Yu, H. Gao, X. Niu, Y. Wang, X. Zhao, G. Sun and D. Li, Gamma-ray irradiation assisted polyacrylamide gel synthesis of scheelite type $BaWO_4$ phosphors and its colorimetric, optical and photoluminescence properties, *ChemistrySelect*, 2020, **5**(34), 10599–10606.

27 P. Liu, Y. Xu, Y. Zhang, L. Han, H. Lian and J. Lin, Epitaxial growth of lattice-matched $BaWO_4/CH_3NH_3PbX_3$ (X = Cl, Br, I) hetero-micro/nanostructure with suppressed halide ion migration, *Adv. Opt. Mater.*, 2023, **11**(12), 2300440.

28 P. Liu, Y. Xu, B. Li, Y. Zhang, H. Lian and J. Lin, Structural engineering of $BaWO_4/CsPbX_3/CsPb_2X_5$ (X = Cl, Br, I) heterostructures towards ultrastable and tunable photoluminescence, *Nano Res.*, 2024, **17**(3), 1636–1645.

29 P. Shi, Y. Ding, B. Ding, Q. Xing, T. Kodalle, C. M. Sutter-Fella, I. Yavuz, C. Yao, W. Fan, J. Xu, Y. Tian, D. Gu, K. Zhao, S. Tan, X. Zhang, L. Yao, P. J. Dyson, J. L. Slack, D. Yang, J. Xue, M. K. Nazeeruddin, Y. Yang and R. Wang, Oriented nucleation in formamidinium perovskite for photovoltaics, *Nature*, 2023, **620**(7973), 323–327.

30 L. Fang, Y. Guo, S. Zhang, Y. Lv, Y. Xue, X. Bai, J. Li, C. Lai and Y. Wang, Influence of transition metal substitution on $Cs_2AgBiBr_6/M_3C_2$ (M = Ti, V, Cr, Zr, Nb, Mo, Hf, Ta, and W) interfaces: First-principles and experimental studies, *Appl. Surf. Sci.*, 2023, **641**, 158538.

31 Y. Guo, L. Fang, Q. Li, X. Bai, Y. Xue, C. Lai and Y. Wang, Insight into the interface engineering between methylammonium lead halide perovskites and gallium oxide: A first-principles approach, *Phys. Chem. Chem. Phys.*, 2023, **25**(46), 31804–31812.

32 Y. Ma, G. Han, M. Yang, M. Guo, Y. Xiao, Y. Guo and W. Hou, Inhibiting Li^+ migration by thenoyltrifluoroacetone toward efficient and stable perovskite solar cells, *Inorg. Chem. Front.*, 2023, **10**(8), 2294–2303.

33 M. Zhang, Q. Luo, C. Sheng, D. Cao, X. Chen and H. Shu, Space-confined growth of large-mismatch $CsPb(Br_xCI_{1-x})_3$/GaN heterostructures with tunable band alignments and optical properties, *Inorg. Chem. Front.*, 2022, **9**(18), 4661–4670.

34 P. E. Blöchl, Projector augmented-wave method, *Phys. Rev. B: Condens. Matter Mater. Phys.*, 1994, **50**(24), 17953–17979.

35 G. Kresse and D. Joubert, From ultrasoft pseudopotentials to the projector augmented-wave method, *Phys. Rev. B: Condens. Matter Mater. Phys.*, 1999, **59**(3), 1758–1775.

36 G. Kresse and J. Furthmüller, Efficiency of *ab initio* total energy calculations for metals and semiconductors using a plane-wave basis set, *Comput. Mater. Sci.*, 1996, **6**(1), 15–50.

37 G. Kresse and J. Furthmüller, Efficient iterative schemes for ab initio total-energy calculations using a plane-wave basis set, *Phys. Rev. B: Condens. Matter Mater. Phys.*, 1996, **54**(16), 11169–11186.

38 J. P. Perdew, K. Burke and M. Ernzerhof, Generalized gradient approximation made simple, *Phys. Rev. Lett.*, 1996, **77**(18), 3865–3868.

39 M. Methfessel and A. T. Paxton, High-precision sampling for Brillouin-zone integration in metals, *Phys. Rev. B: Condens. Matter Mater. Phys.*, 1989, **40**(6), 3616–3621.

40 H. J. Monkhorst and J. D. Pack, Special points for Brillouin-zone integrations, *Phys. Rev. B: Solid State*, 1976, **13**(12), 5188–5192.

41 S. Grimme, Semiempirical GGA-type density functional constructed with a long-range dispersion correction, *J. Comput. Chem.*, 2006, **27**(15), 1787–1799.

42 K. Momma and F. Izumi, VESTA 3 for three-dimensional visualization of crystal, volumetric and morphology data, *J. Appl. Crystallogr.*, 2011, **44**(6), 1272–1276.

43 S. P. Culver, M. J. Greaney, A. Tinoco and R. L. Brutchey, Low-temperature synthesis of homogeneous solid solutions of scheelite-structured $Ca_{1-x}Sr_xWO_4$ and $Sr_{1-x}Ba_xWO_4$ nanocrystals, *Dalton Trans.*, 2015, **44**(33), 15042–15048.

44 Y. Xie, B. Peng, I. Bravić, Y. Yu, Y. Dong, R. Liang, Q. Ou, B. Monserrat and S. Zhang, Highly efficient blue-emitting $CsPbBr_3$ perovskite nanocrystals through neodymium doping, *Adv. Sci.*, 2020, **7**(20), 2001698.

45 S. Shahrokhi, M. Dubajic, Z.-Z. Dai, S. Bhattacharyya, R. A. Mole, K. C. Rule, M. Bhadbhade, R. Tian, N. Mussakhanuly, X. Guan, Y. Yin, M. P. Nielsen, L. Hu, C.-H. Lin, S. L. Y. Chang, D. Wang, I. V. Kabakova, G. Conibeer, S. Bremner, X.-G. Li, C. Cazorla and T. Wu, Anomalous structural evolution and glassy lattice in mixed-halide hybrid perovskites, *Small*, 2022, **18**(21), 2200847.

46 J. E. Castellanos-Águila, L. Lodeiro, E. Menéndez-Proupin, A. L. Montero-Alejo, P. Palacios, J. C. Conesa and P. Wahnón, Atomic-scale model and electronic structure of $Cu_2O/CH_3NH_3PbI_3$ interfaces in perovskite solar cells, *ACS Appl. Mater. Interfaces*, 2020, **12**(40), 44648–44657.

47 A. Pecoraro, A. De Maria, P. Delli Veneri, M. Pavone and A. B. Muñoz-García, Interfacial electronic features in methyl-ammonium lead iodide and p-type oxide heterostructures: new insights for inverted perovskite solar cells, *Phys. Chem. Chem. Phys.*, 2020, **22**(48), 28401–28413.

48 H. Zhang, J. Wang, W. Huang, L. Wang and Z. Lu, Interface bonding and failure mechanism of Ti(001)/Si(001) and TiO_2(001)/Si(001) interfaces: A first-principles study, *Surf. Interfaces*, 2022, **30**, 101833.

49 M. W. Stoltzfus, P. M. Woodward, R. Seshadri, J.-H. Klepeis and B. Bursten, Structure and bonding in $SnWO_4$, $PbWO_4$, and $BiVO_4$: Lone pairs vs inert pairs, *Inorg. Chem.*, 2007, **46**(10), 3839–3850.

50 X. Gong, O. Voznyy, A. Jain, W. Liu, R. Sabatini, Z. Piontkowski, G. Walters, G. Bappi, S. Nokhrin, O. Bushuyev, M. Yuan, R. Comin, D. McCamant, S. O. Kelley and E. H. Sargent, Electron–phonon interaction in efficient perovskite blue emitters, *Nat. Mater.*, 2018, **17**(6), 550–556.

51 C. Quarti, F. De Angelis and D. Beljonne, Influence of surface termination on the energy level alignment at the $CH_3NH_3PbI_3$ perovskite/C60 interface, *Chem. Mater.*, 2017, **29**(3), 958–968.

52 B. Du, Q. Wei, Y. Cai, T. Liu, B. Wu, Y. Li, Y. Chen, Y. Xia, G. Xing and W. Huang, Crystal face dependent charge carrier extraction in TiO_2/perovskite heterojunctions, *Nano Energy*, 2020, **67**, 104227.
53 Y. Guo, Y. Xue and L. Xu, Interfacial interactions and enhanced optoelectronic properties of GaN/perovskite heterostructures: Insight from first-principles calculations, *J. Mater. Sci.*, 2021, **56**(19), 11352–11363.
54 A. Giampietri, G. Drera and L. Sangaletti, Band alignment at heteroepitaxial perovskite oxide interfaces. Experiments, methods, and perspectives, *Adv. Mater. Interfaces*, 2017, **4**(11), 1700144.
55 D. Q. Fang and S. L. Zhang, Theoretical prediction of the band offsets at the ZnO/anatase TiO_2 and GaN/ZnO heterojunctions using the self-consistent ab initio DFT/GGA-1/2 method, *J. Chem. Phys.*, 2016, **144**(1), 014704.
56 M. Tyagi, S. G. Singh, A. K. Chauhan and S. C. Gadkari, First principles calculation of optical properties of $BaWO_4$: A study by full potential method, *Phys. B*, 2010, **405**(21), 4530–4535.
57 R. Lindblad, D. Bi, B.-w. Park, J. Oscarsson, M. Gorgoi, H. Siegbahn, M. Odelius, E. M. J. Johansson and H. Rensmo, Electronic Structure of $TiO_2/CH_3NH_3PbI_3$ perovskite solar cell interfaces, *J. Phys. Chem. Lett.*, 2014, **5**(4), 648–653.
58 M. Cao, Y. Damji, C. Zhang, L. Wu, Q. Zhong, P. Li, D. Yang, Y. Xu and Q. Zhang, Low-dimensional-networked cesium lead halide perovskites: properties, fabrication, and applications, *Small Methods*, 2020, **4**(12), 2000303.
59 P. Yadav, P. Dev Bhuyan, S. K. Rout, Y. Sonvane, S. K. Gupta and E. Sinha, Correlation between experimental and theoretical study of scheelite and wolframite-type tungstates, *Mater. Today Commun.*, 2020, **25**, 101417.
60 G. Ghosh, B. Jana, S. Sain, A. Ghosh and A. Patra, Influence of shape on the carrier relaxation dynamics of $CsPbBr_3$ perovskite nanocrystals, *Phys. Chem. Chem. Phys.*, 2019, **21**(35), 19318–19326.
61 S. Thawarkar, P. J. S. Rana, R. Narayan and S. P. Singh, Ni-doped $CsPbBr_3$ perovskite: Synthesis of highly stable nanocubes, *Langmuir*, 2019, **35**(52), 17150–17155.
62 D. Rangappa, T. Fujiwara and M. Yoshimura, Synthesis of highly crystallized $BaWO_4$ film by chemical reaction method at room temperature, *Solid State Sci.*, 2006, **8**(9), 1074–1078.
63 E. Hannachi, Y. Slimani, M. I. Sayyed and K. G. Mahmoud, Scheelite-type $BaWO_4$ doped with Ho_2O_3 oxide as a promising lead-free shield for gamma rays: Structural, optical properties, and radiation attenuation efficiency, *Mater. Sci. Semicond. Process.*, 2023, **167**, 107802.
64 M. I. A. Abdel Maksoud, M. A. Youssef and H. S. Hassan, Evaluation of barium tungstate nanocrystals for the sorption of radioactive cobalt and europium from aqueous solutions, *Sci. Rep.*, 2023, **13**(1), 21570.
65 L. M. Wheeler, E. M. Sanehira, A. R. Marshall, P. Schulz, M. Suri, N. C. Anderson, J. A. Christians, D. Nordlund, D. Sokaras, T. Kroll, S. P. Harvey, J. J. Berry, L. Y. Lin and J. M. Luther, Targeted ligand-exchange chemistry on cesium lead halide perovskite quantum dots for high-efficiency photovoltaics, *J. Am. Chem. Soc.*, 2018, **140**(33), 10504–10513.
66 H. Yang, W. Yin, W. Dong, L. Gao, C.-H. Tan, W. Li, X. Zhang and J. Zhang, Enhancing the light-emitting performance and stability in $CsPbBr_3$ perovskite quantum dots via simultaneous doping and surface passivation, *J. Mater. Chem. C*, 2020, **8**(41), 14439–14445.
67 Y. Mao and S. S. Wong, General, room-temperature method for the synthesis of isolated as well as arrays of single-crystalline ABO_4-type nanorods, *J. Am. Chem. Soc.*, 2004, **126**(46), 15245–15252.